Far-field superresolution shape reconstruction of objects using level-set-based geometrical full-waveform inversion

Xiao Yin and Fan Shi[*]

Department of Mechanical and Aerospace Engineering, The Hong Kong University of Science and Technology, Sai Kung, Hong Kong SAR

Far-field wave imaging and inversion of objects with dimension and spacing much smaller than the wavelength are very difficult because of the well-known diffraction limit. The task becomes more challenging for quantitative shape reconstruction of closely spaced subwavelength impenetrable scatterers. Apart from the classic resolution limit, complex wave interaction including evanescent waves among impenetrable objects can be strong, but it is difficult to be fully utilized for correct shape inversion although it contains critical resolution information. Here we tackle this problem by proposing a level-set-based geometrical full-waveform inversion method. It makes full use of wave physics to directly reconstruct subwavelength objects of arbitrary shapes separated within half a wavelength. Shape reconstruction is controlled by the geometrical boundary gradient calculated from the finite-element formulation, and the important role of wave interaction among objects in the inversion is demonstrated. The boundaries of the objects are represented using the level-set method, allowing for reconstruction of multiple objects simultaneously. Numerical examples and experiments of ultrasonic waves in solid samples demonstrate that the method successfully reconstructs closely spaced subwavelength objects with far-field measurements, and the resolution is shown to be within a fraction of wavelength. This level of accuracy can be very useful in subsurface imaging applications such as ultrasonic nondestructive evaluation, medical diagnosis, and electromagnetic sensing.

I. INTRODUCTION

The resolution of far-field wave imaging is well known to be hindered by the fundamental diffraction limit established by Lord Rayleigh; the minimum resolvable size of objects is of the order of probing wavelength λ [1]. In an ideal full-view setup the resolution limit is shown to be $\lambda/2$ [2]. To bypass the diffraction limit in common far-field imaging, monumental advances have been made in near-field microscopy [3,4] to allow for superresolution imaging. This is achieved by taking a measurement very close to the object surface to capture the evanescent waves that contain deep-subwavelength features.

However, more often the measurements can only be taken in the far field, for instance, for imaging the subsurface world, such as seismic exploration, biomedical imaging, and ultrasonic defect and/or material characterization. The evanescent waves die out beyond one wavelength, which severely limits the resolution of conventional imaging approaches such as beamforming [5] and diffraction tomography [6]. Recently researchers have made significant progress in developing methods to break the resolution limit. For example, metamaterials such as

superlens [7] and local resonant metalens [8] were used to convert evanescent waves into those that can propagate into the far field, and images with subwavelength features were obtained. However, auxiliary materials need to be placed near the object, which is not feasible for subsurface imaging. Superoscillation phenomena were exploited to achieve subwavelength focusing and imaging results [9], but they suffer from relatively low signal-to-noise ratio due to strong sidelobes. Besides, superresolution fluorescent microscopy techniques [10] have been developed based on stimulated emission to visualize biological cells.

Besides the above techniques, researchers have also investigated superresolution imaging and/or detection algorithms based on decomposing the far-field operator [11], such as the factorization method (FM) [12], time-reversed multiple signal classification [13], and the linear sampling method [14]. Small eigenvalues and the corresponding eigenvectors refer to high-order scattering events, which can be used to reveal important subwavelength information. However, they still have limited accuracy for reconstructing the exact shapes of closely spaced subwavelength objects [15], and their performance is sensitive to noise.

The principal notion of resolution is the capability of identification of two small objects (e.g., point scatterers)

---

*maefanshi@ust.hk

024055-1

close to each other in an image. Beyond this, an important but more challenging topic is the quantitative reconstruction of one or several closely spaced small objects of arbitrary shapes (spacing $\leq \lambda/2$). This is particularly useful for describing impenetrable or strong scatterers (e.g., voids), whose geometrical features provide key information in applications including ultrasonic nondestructive evaluation [16], seismic inversion [17], underwater acoustic sensing [18], and biomedical imaging [19]. However, superresolution shape reconstruction of impenetrable objects has been so far rarely tackled successfully. Apart from the well-known diffraction resolution limit, wave interaction among impenetrable scatterers and their geometrical features can be strong and complex, and proper use of them for correct shape inversion is difficult for existing imaging algorithms.

Full-waveform inversion (FWI), originally developed within geophysics, has recently become popular in different fields of wave imaging [20,21]. It iteratively reconstructs physical parameters until the modeled wave field matches with measurements. Traditionally, the majority of FWI algorithms are designed to produce an image of material properties of penetrable scatterers, such as wave speed [22], modulus [23], or mass density [24], but they have difficulty in achieving target convergence for shape inversion of strong impenetrable objects [25]. In addition, the resolution of most conventional approaches still obeys the diffraction limit [20]. More recently, a method called geometrical full-waveform inversion (GFWI) has been developed [26], which aims at directly inverting the geometries of an impenetrable object. GFWI has been successfully applied in one-dimensional guided wave mapping of corrosion [27]. It has also been applied for ultrasonic characterization of cracks [28], although the shape inversion in that study was limited to a large single defect with a regular shape.

In this article, we show that far-field superresolution reconstruction of closely spaced subwavelength objects with arbitrary shapes can be realized. This is achieved by applying the GFWI approach combined with the level-set method, which accurately captures the topological variation of several objects during the inversion process. Hence the method allows for examining the resolution by inverting small objects separated within half a wavelength. All the wave scattering physics is included in the inversion process to realize accurate reconstruction. The wave interaction among objects is shown to be non-negligible and plays important roles during shape inversion. As illustrated in Fig. 1(a), the inner boundaries of closely spaced objects are not directly probed by the incident bulk waves. They can be only recovered via the use of far-field measurement of indirect waves produced from inner boundaries, including evanescent waves propagating along the surface and mode conversion between surface and bulk waves. Correctly revealing the inner boundaries is critical

to demonstrate the capability of superresolution imaging. While the proposed method is generic to be applied by acoustic, electromagnetic, and seismic wave communities, in this article we choose the cases of ultrasonic probing of voids and defects embedded in solid media.

The article is organized as follows. Section II briefly introduces the level-set-based GFWI method. The success of the method in achieving superresolution shape reconstruction is supported by numerical examples in Sec. III including both full-view and limited-view imaging setups. The capability is further demonstrated in one case of shape inversion of multiple irregular voids in Sec. IV, and the importance of taking strong wave interaction among voids into the inversion process is discussed. An experiment of reconstructing two subwavelength voids with an ultrasonic phased array is presented in Sec. V to further show the applicability of the proposed method in practice. Finally, we draw concluding remarks in Sec. VI.

II. WAVEFORM INVERSION APPROACH

In this section, the proposed level-set-based GFWI method is introduced and a flowchart illustrating the approach is shown in Fig. 1(b). An initial geometrical model is given and we assign an initial level-set function according to the shape. The initial model is then used to run the GFWI method to calculate the geometrical boundary gradient, and all the wave mechanisms are used during both forward and inverse modeling. The boundary gradient values are then used to update the level-set function, whose zero-level-set contour is extracted as the boundaries of the updated shape. The updated shape is used in the next iteration of GFWI to evolve the shape, and the iterations are run until the modeled scattering wave forms match with the measurements. The details of the method are illustrated in the following.

A. Geometrical boundary gradient

FWI gradually reconstructs the subsurface model by minimizing the mismatch between simulated and observed wave forms. The corresponding cost function can be written as

$$C(\mathbf{m}) = \int_0^\infty \sum_j F\left[\mathbf{u}_j(t), \mathbf{u}_{\mathrm{mod},j}(\mathbf{m},t)\right] dt, \qquad (1)$$

where $\mathbf{u}_j(t)$ and $\mathbf{u}_{\mathrm{mod},j}(\mathbf{m},t)$ represent the measurement and the simulated data received at the jth sensor at time t, respectively. $\mathbf{m}$ is the geometrical model vector describing the shapes of the objects to be reconstructed and $F\left[\mathbf{u}_j(t), \mathbf{u}_{\mathrm{mod},j}(\mathbf{m},t)\right]$ is a function that measures the mismatch between $\mathbf{u}_j$ and $\mathbf{u}_{\mathrm{mod},j}(\mathbf{m})$. In this article, we choose F as an $L2$ norm difference function, i.e., $F\left[\mathbf{u}_j(t), \mathbf{u}_{\mathrm{mod},j}(\mathbf{m},t)\right] = [\mathbf{u}_{\mathrm{mod},j}(\mathbf{m},t) - \mathbf{u}_j(t)]^T[\mathbf{u}_{\mathrm{mod},j}(\mathbf{m},t) - \mathbf{u}_j(t)]$. For simplicity,
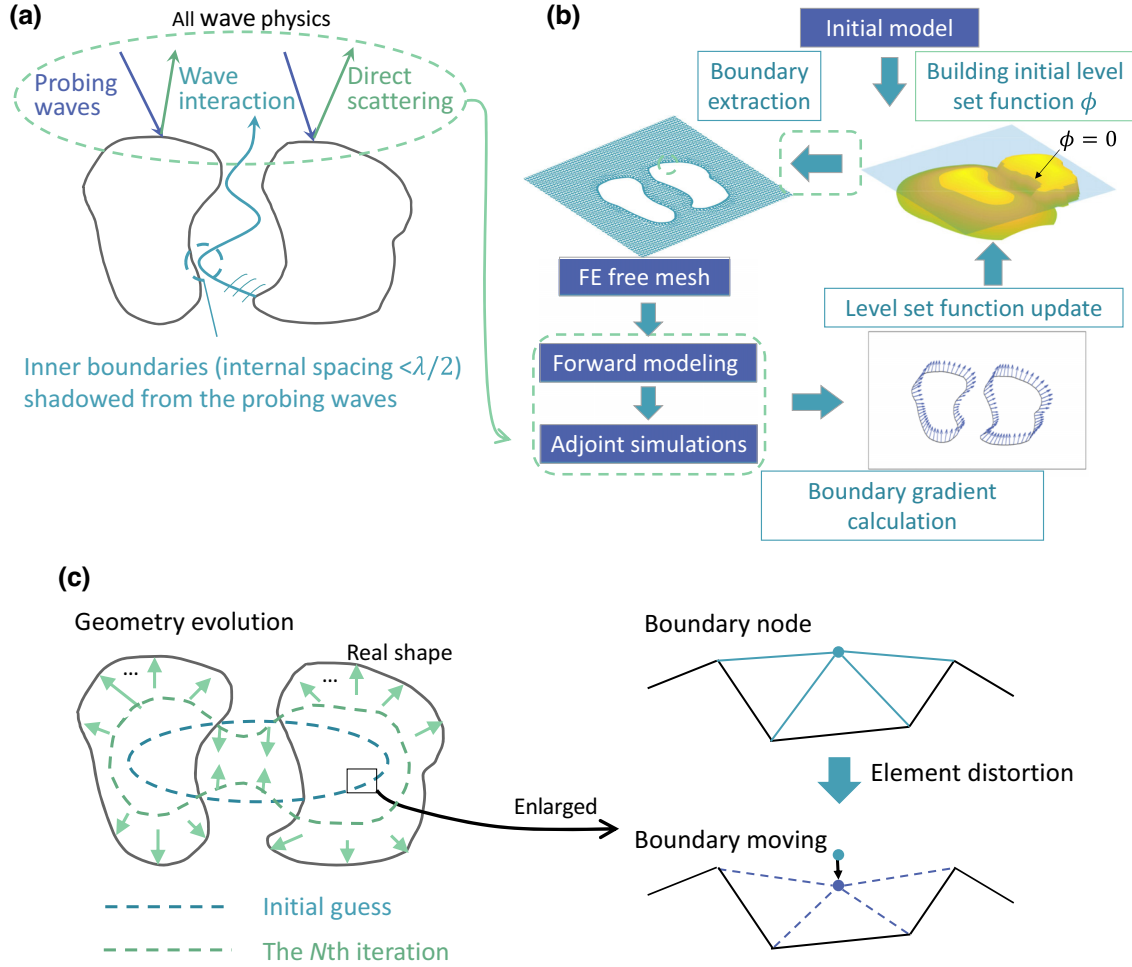
FIG. 1. Illustration of the level-set-based GFWI method. (a) Full-wave physics is utilized in the shape inversion. To reveal inner boundaries that are shadowed from direct probing waves, the complex interior wave interaction among the voids needs to be used. (b) Flow sketch of the level-set-based GFWI method. The update of the boundary contour (arrow within a dotted square) is caused by the distortion of the elements attached to the boundary as sketched in (c). (c) Illustration of geometry evolution. The elements are deformed during inversion.

we omit the parameter t from now on. Using the chain rule, we can obtain the gradient regarding the ith parameter m_i as

$$\frac{\partial C}{\partial m_i} = \int_0^\infty 2 \sum_j \left(\frac{\partial \mathbf{u}_{\mathrm{mod},j}}{\partial m_i} \right)^T \mathbf{r}_j \, dt, \qquad (2)$$

where $\mathbf{r}_j$ is the residual between the calculated and observed data, i.e., $\mathbf{r}_j = \mathbf{u}_{\mathrm{mod},j} - \mathbf{u}_j$. m_i is the ith parameter of $\mathbf{m}$ and $\partial \mathbf{u}_{\mathrm{mod},j}/\partial m_i$ is the sensitivity kernel. To calculate the sensitivity kernel, we first write the second-order finite-element (FE) explicit equation for elastic waves as

$$\mathbf{M}\ddot{\mathbf{u}} + \mathbf{C}\dot{\mathbf{u}} + \mathbf{K}\mathbf{u} = \mathbf{f}, \qquad (3)$$

where $\mathbf{K}$, $\mathbf{C}$, and $\mathbf{M}$ are the stiffness, damping, and mass matrices, respectively. $\mathbf{f}$ is the external applied force. $\ddot{\mathbf{u}}$, $\dot{\mathbf{u}}$,

and $\mathbf{u}$ are the acceleration, velocity, and displacement vectors. Here we assume that no damping exists in the region of imaging, and the external force $\mathbf{f}$ is not affected by any model perturbations. Differentiating Eq. (3) with regard to m_i and rearranging the terms lead to

$$\frac{\partial \mathbf{u}_{\mathrm{mod},j}}{\partial m_i} = -\mathbf{Q}\left(\frac{\partial \mathbf{K}}{\partial m_i}\mathbf{u} + \frac{\partial \mathbf{M}}{\partial m_i}\ddot{\mathbf{u}} \right), \qquad (4)$$

where $\mathbf{Q} = (\mathbf{M} + \mathbf{K}(\partial^2)/\partial t^2)^{-1}$, and it denotes the numerical operator to solve the forward FE equations of elastic wave propagation without damping. In Eq. (4), the two terms $\partial \mathbf{K}/\partial m_i$ and $\partial \mathbf{M}/\partial m_i$ imply the change in the stiffness and mass matrices due to the perturbation in the shape parameter m_i. This is caused by the deformation of the elements attached to the boundary. To obtain $\partial \mathbf{K}/\partial m_i$ and $\partial \mathbf{M}/\partial m_i$, we need to calculate the shape derivatives

$\partial \mathbf{K}_{\mathrm{el}}/\partial \mathbf{x}$ and $\partial \mathbf{M}_{\mathrm{el}}/\partial \mathbf{x}$ where $\mathbf{x}$ refers to the global coordinates of the node. In this way, the scatterer will evolve its boundary from an initial model following the negative boundary gradients and eventually match the true shape after a few iterations.

Substituting Eq. (4) back into Eq. (2) gives

$$\frac{\partial C}{\partial m_i} = -\int_0^\infty 2 \sum_j \left[\mathbf{Q} \left(\frac{\partial \mathbf{K}}{\partial m_i} \mathbf{u} + \frac{\partial \mathbf{M}}{\partial m_i} \ddot{\mathbf{u}} \right) \right]^T \mathbf{r}_j \, dt. \quad (5)$$

This equation indicates that the forward models need to be run multiple times corresponding to each model parameter. To simplify the computation, we can use Parseval's theorem and obtain the adjoint operator in the time domain and get the final expression of the boundary gradient as

$$\begin{aligned}
\frac{\partial C}{\partial m_i} &= -\int_0^\infty 2 \sum_j \left[\mathbf{Q} \left(\frac{\partial \mathbf{K}}{\partial m_i} \mathbf{u} + \frac{\partial \mathbf{M}}{\partial m_i} \ddot{\mathbf{u}} \right) \right]^T \mathbf{r}_j \, dt \\
&= -\int_0^\infty 2 \sum_j \left[\hat{\mathbf{Q}} \left(\frac{\partial \mathbf{K}}{\partial m_i} - \omega^2 \frac{\partial \mathbf{M}}{\partial m_i} \right) \hat{\mathbf{u}} \right]^T \hat{\mathbf{r}}_j \, df \\
&= -\int_0^\infty \sum 2 (\hat{\mathbf{Q}}^T \hat{\mathbf{r}}_j)^T \left(\frac{\partial \mathbf{K}}{\partial m_i} - \omega^2 \frac{\partial \mathbf{M}}{\partial m_i} \right) \hat{\mathbf{u}} \, df \\
&= -\int_0^\infty \sum 2 (\mathbf{Q}^\dagger \mathbf{r}_j)^\dagger \left(\frac{\partial \mathbf{K}}{\partial m_i} \mathbf{u} + \frac{\partial \mathbf{M}}{\partial m_i} \ddot{\mathbf{u}} \right) dt, \quad (6)
\end{aligned}$$

where the hat denotes the corresponding quantity after performing a Fourier transform. The superscript dagger represents a time reversal operator of the signal, and $\mathbf{Q}^\dagger \mathbf{r}_j$ refers to backpropagating the time-reversed residual signals into the domain where $\mathbf{m}$ is located.

B. Level-set method

In this article, we use the level-set method [29] to represent the shapes of one or multiple voids with arbitrary shapes. This method defines a level-set function to implicitly describe the geometry. It can always provide a clear boundary during shape evolution and hence is widely used for solving topology-optimization-related problems [30,31]. The most important advantage of the level set is its stability in handling topological variations such as splitting one void into multiple voids and vice versa, in comparison with approaches using explicit parameterization schemes. This capability is particularly useful in the application here to invert closely spaced tiny voids.

For a 2D problem, a level-set function Φ maps from $\mathbb{R}^2$ to $\mathbb{R}$, and a level set is the set of coordinates when Φ is a constant value, i.e., $\Gamma = \{\mathbf{x} | \Phi(\mathbf{x}) = a\}$. The level-set

function Φ usually satisfies the following expressions:

$$\begin{aligned}
\Phi(\mathbf{x}) &> 0 \, \mathbf{x} \in D, \\
\Phi(\mathbf{x}) &= 0 \, \mathbf{x} \in \partial\Omega, \quad (7) \\
\Phi(\mathbf{x}) &< 0 \, \mathbf{x} \in \Omega,
\end{aligned}$$

where D represents the area inside voids, $\partial\Omega = \Gamma(0)$ is the boundary of voids (i.e., the zero level set), and Ω is the rest of the domain outside the voids as shown in Fig. 2. A level-set function can be parameterized with different basis functions in order to improve the numerical accuracy [30]. In this article, we choose to use the MultiQuadratic (MQ) spline, which is a globally supported radial basis function (RBF) and converges fast in topology optimization [32]. The MQ spline can be written as

$$g_i(\mathbf{x}) = \sqrt{\|\mathbf{x} - \mathbf{x}_i\|^2 + c^2}, \quad (8)$$

where $\mathbf{x}_i$ is the coordinate vector of the ith grid point discretized for defining Φ and c is the corresponding shape parameter, which is usually assumed to be a small constant. If we consider the geometry evolution along the pseudotime t, the corresponding level-set function can be expressed as

$$\Phi(\mathbf{x}, t) = \sum_{i=1}^n \alpha_i(t) g_i(\mathbf{x}) + p(\mathbf{x}, t), \quad (9)$$

where $\alpha_i(t)$ is the expansion coefficient for the ith grid point at pseudotime t and $p(\mathbf{x}, t)$ is a first-degree polynomial to account for the constant and linear part of Φ, which can be written as

$$p(\mathbf{x}, t) = p_0(t) + p_1(t)x + p_2(t)y. \quad (10)$$

To ensure a unique RBF interpolation of the level-set function, the expansion coefficients $\alpha(t)$ must satisfy the following requirement [32]:

$$\sum_{i=1}^n \alpha_i(t) = 0, \quad \sum_{i=1}^n \alpha_i(t)x_i = 0, \quad \sum_{i=1}^n \alpha_i(t)y_i = 0. \quad (11)$$

By combining Eqs. (9) and (10), the level-set function with the above constraints can be written in the matrix form as

$$\Phi(t) = \mathbf{L}\alpha(t), \quad (12)$$

where $\mathbf{L}$ is a matrix containing elements of $g_i(\mathbf{x})$ and $\alpha(t)$ is a vector composed of $\alpha_i(t)$.
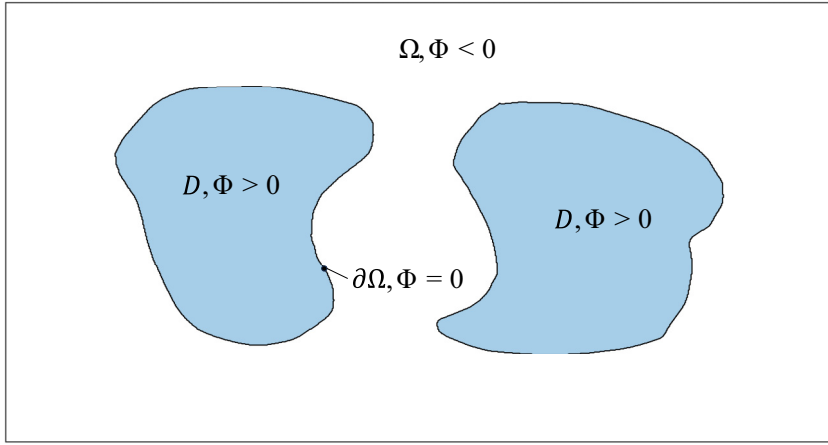
FIG. 2. Illustration of the level-set function Φ, with D denoting the impenetrable objects, $\partial\Omega$ representing the boundaries of the objects, and Ω standing for the rest of the domain.

We choose the initial level-set function to be the signed distance function regarding the boundary [33]:

$$\Phi(\mathbf{x}_i, t = 0) = \inf_{\mathbf{x}_b \in \partial\Omega} \|\mathbf{x}_i - \mathbf{x}_b\|^2 S(\Phi_0), \qquad (13)$$

where

$$S(\Phi) = \frac{\Phi}{\sqrt{\Phi^2 + \delta^2}}, \Phi_0(\mathbf{x}_i) = \begin{cases} 1, & \mathbf{x}_i \in D + \partial\Omega \\ -1, & \mathbf{x}_i \in \Omega. \end{cases}$$

The governing equation for the evolution of the level-set function is given by Ref. [31], and here we provide its discretized form as

$$\frac{\partial \Phi(\mathbf{x}_i, t)}{\partial t} + V \cdot \nabla \Phi(\mathbf{x}_i, t) = w\kappa |\nabla \Phi(\mathbf{x}_i, t)|, \qquad (14)$$

where V is the directional force acting on the level-set surfaces. Using the steepest descent method, the acting force in Eq. (14) can be set as the negative boundary gradient calculated in GFWI, i.e., $V = -\nabla C(\mathbf{x}_b)$. $\kappa = \nabla \cdot \nabla \Phi / |\nabla \Phi|$ is the surface curvature and $w > 0$ is the curvature weight for smoothing the surfaces. Equation (14) can be solved numerically for instance using the finite-difference scheme. Note that the boundary gradient $\nabla C(\mathbf{x}_b)$ needs to be extended from $\partial\Omega$ to the whole area. To simplify this procedure, we define the normal directional force to the boundary as

$$V_n = -\nabla C(\mathbf{x}_b) \cdot \frac{(\nabla \mathbf{L})\alpha(t)}{|(\nabla \mathbf{L})\alpha(t)|}. \qquad (15)$$

The extended normal force V_n^{ext} from V_n can be obtained using the following relationship [33,35]:

$$\nabla V_n^{\text{ext}} \cdot \nabla \Phi = 0. \qquad (16)$$

Note that the extrapolation can be optimized so that V_n^{ext} has nonzero values only in a small neighborhood of $\partial\Omega$.

III. NUMERICAL SIMULATION

Now we perform 2D numerical simulations to evaluate the performance of the level-set-based GFWI method. The examples are taken from ultrasonic imaging of one or more subwavelength voids in solid bulk media. The simulations are conducted using an accelerated elastic wave FE software package, Pogo, based on multiple graphics processing units (GPUs) developed by Huthwaite [36]. The solid medium is aluminum with a density of 2700 kg/m^3, Young's modulus of 70 GPa, and Poisson's ratio of 0.33. An ultrasonic array with multiple elements is simulated, and each sensor serves as both transmitter and receiver to perform a full matrix capture of scattered waves. The incident wave signal is a two-cycle Hann-windowed tone burst with a center frequency of 2.25 MHz. The corresponding compressional (P) and shear (S) wavelengths are $\lambda_p = 2.75$ mm and $\lambda_s = 1.39$ mm, respectively. To fully capture the exact shapes of the voids and defects, all the FE models are meshed using linear triangular elements with a Delaunay-based automatic algorithm. The element size is set to be 0.05 mm (approximately $\lambda_p/60$) to ensure convergence and the time step is set based on the Courant criterion [37].

Two common array configurations are considered in the numerical simulations. We first consider scatterers surrounded by a circular array, which forms an ideal full-aperture imaging setup shown in Fig. 3(a). The circular array has a radius of 15 mm (approximately $5.5\lambda_p$) with 81 sensors, separated by an interval of 1.16 mm ($< \lambda_p/2$). Three numerical examples are evaluated under the full-aperture setup: a void in a pentagram shape, two semicircular voids, and four triangular voids separated well below half a wavelength, as shown in Figs. 3(b)–3(d). Note that the case of four voids and the role of wave interaction will be discussed separately in the next section. In the second configuration, a linear array composed of 64 elements is placed on the top of the sample, and the bottom surface (e.g., backwall) is included in the model. The pitch of the array is 0.8 mm ($< \lambda_p/2$). The array has a limited aperture
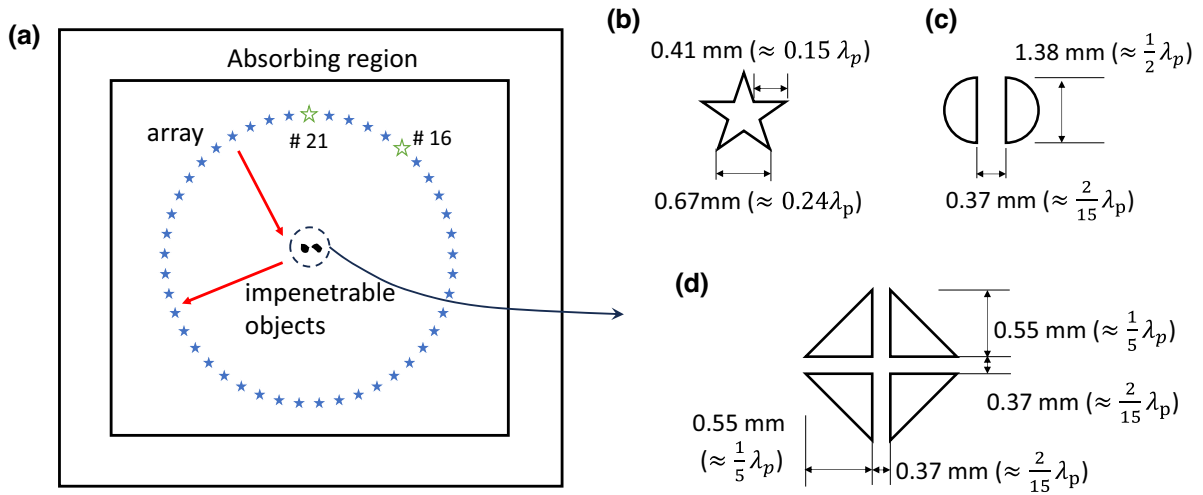
FIG. 3. The full-view array imaging configuration. (a) The simulation setup. (b) A void with a pentagram shape. (c) Two subwavelength semicircular voids separated within half a wavelength. (d) Four closely spaced triangular voids.

width and it is closer to the experimental setup. The scatterers in all the examples are set to be in the subwavelength scale, and their shapes are difficult to reconstruct using existing imaging methods.

A. A subwavelength void in a pentagram shape

For the full-aperture simulations with a circular array, each sensor is modeled as six adjacent nodes connected at the center node, forming a regular hexagon. Radial forces are applied on the six nodes to excite purely circular P waves. The dimension of the whole FE domain is 60×60 mm^2. Absorbing regions with the stiffness reduction method [38] are placed on the four sides of the FE domain, with a thickness of 5 mm (approximately $1.82\lambda_p$). In the first numerical example, we reconstruct a subwavelength void in a pentagram shape as sketched in Fig. 3(b), with its center positioned at (0 mm, −0.17 mm). The side length of the pentagram is 0.41 mm (approximately $0.15\lambda_p$), and the distance between two adjacent vertices is 0.67 mm (approximately $0.24\lambda_p$). The main geometrical features are only a fraction of the wavelength.

This case demonstrates the generalizability of the proposed method in reconstructing the complex shape of a subwavelength impenetrable scatterer. Figures 4(a) and 4(b) show the array images of the void using conventional total focusing method (TFM) and FM, respectively. Both imaging algorithms can only show a vague shape due to limited resolution. After applying the −6-dB threshold method [39] to the TFM image, we can approximately obtain a circular contour centered at the origin with a radius of 0.7 mm as the blue dashed line in Fig. 4(c). This contour is set as the initial model for running the level-set-based GFWI method, and it is different from the true void shape. However, after a few iterations, we see that the proposed method can gradually update the shape and

the final reconstructed model (red line) almost coincides with the true void shape (the black line) in Fig. 4(c). The deep-subwavelength features such as the sharp vertices are accurately reconstructed, showing significantly improved resolution compared with conventional methods. Note that only a rough estimation of the shape is needed for the initial model to start the shape inversion, and the method is robust for reconstructing the true shape.

B. Two semicircular voids

Two closely located small scatterers are usually used to examine imaging resolution. To further show the capability of the method in achieving superresolution, we set two semicircular voids both with a diameter of 1.38 mm (approximately $\lambda_p/2$) in a full-aperture circular array as shown in Fig. 3(c). The inner boundaries of the two voids are separated only by 0.37 mm (approximately $\frac{2}{15}\lambda_p$), which are difficult to be resolved. Figures 5(a) and 5(b) show the array images of the two voids using TFM and FM, respectively. In the TFM image, only one big contour encircling the voids can be observed but their inner boundaries completely disappear. One can vaguely identify two scatterers from the FM image, but the shapes and boundaries can be hardly quantified. Furthermore, for impenetrable scatterers, the probing waves do not see the inner boundary of one void because they are shadowed by the other void. To reveal the inner boundaries, one has to make full use of the wave interaction events among boundaries including evanescent waves and multiple scattering in the forward and inverse models.

By applying the −6-dB threshold method to the TFM image, a rectangular void with a length of 2.1 mm and a width of 1.6 mm can be obtained as shown in Fig. 5(c), whose topology is clearly distinct from the true shape. However, we can use this large void as the initial model
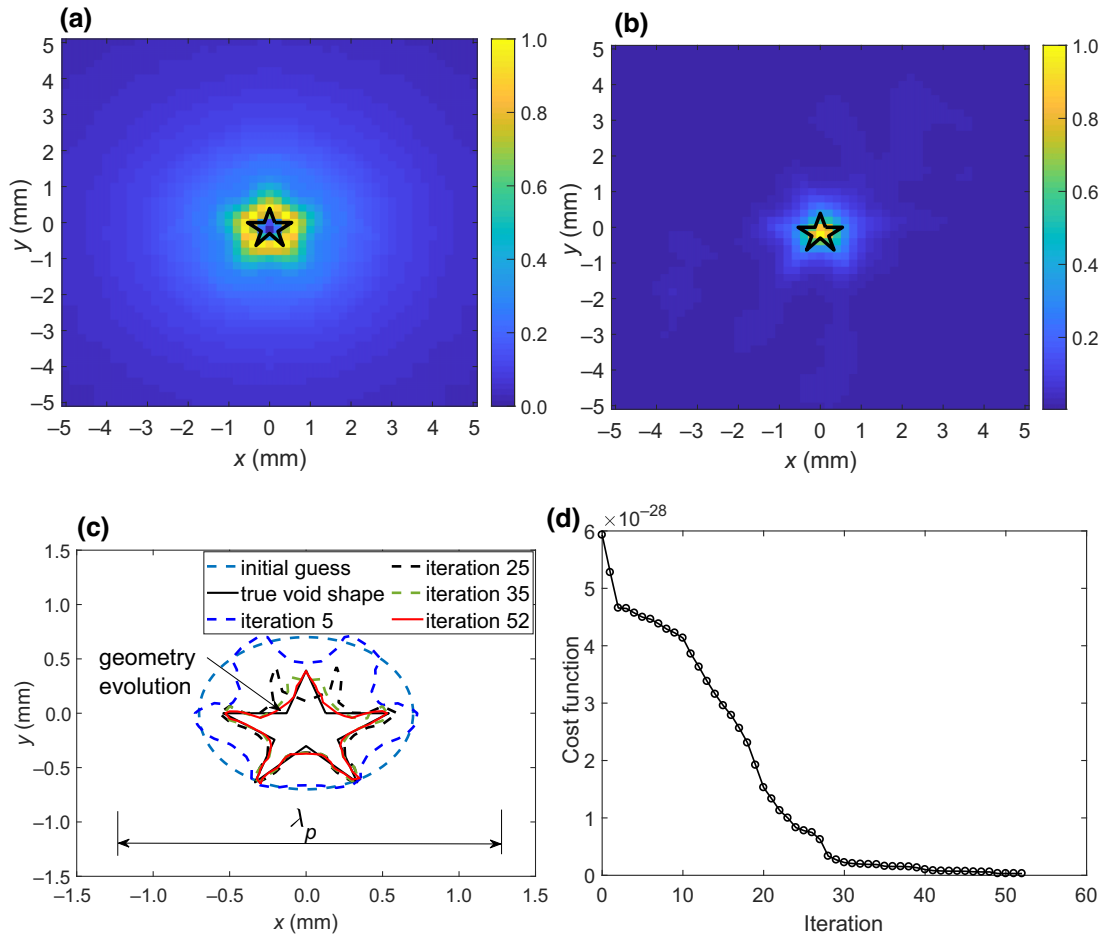
FIG. 4. Reconstruction of a subwavelength void in a pentagram shape. The side length of the void is $0.15\lambda_p$ ($\lambda_p = 2.75$ mm and $\lambda_s = 1.39$ mm). (a) The TFM image. (b) The FM image. (c) The reconstructed shape from the initial guess to the 52nd iteration (final). (d) The cost function.

to start the level-set-based GFWI for shape reconstruction. Figures 5(d)–5(h) show the evolution of the topology at different iterations during inversion and the corresponding convergence of the cost function is plotted in Fig. 5(i). In the first few iterations, the initial rectangular void gradually reduces its extent, and clear indentations can be observed on the top and bottom parts of the boundary. These indentations result in a "dumbbell" shape of the void as shown in Figs. 5(d) and 5(e). The connection area in the dumbbell gradually shrinks and finally breaks from Fig. 5(f) to Fig. 5(g). At the 55th iteration, the inversion successfully leads to a topological change of splitting one void into two small voids in Fig. 5(g). This step is critical to resolving two closely spaced voids and correctly reconstructing their shapes, and it shows the robustness of using the level-set method in capturing topological changes during inversion. The "splitting" action causes a significant drop of the cost function from the 55th to the 56th iteration, as can be observed in Fig. 5(i): major topological variation leads to large perturbations of the wave field and

a dramatic change of the cost function. In the following iterations, the shapes of two voids are further optimized, and the final reconstructed shapes are almost identical to the true geometries as shown in Fig. 5(h). The numerical example here demonstrates that the method can achieve superresolution reconstruction of the two voids, including a clear recovery of the inner boundaries.

C. Limited-aperture setup

In a practical subsurface imaging setup such as ultrasonic defect characterization and seismic imaging, a linear array is placed on the top due to geometrical restriction. The setup poses a limitation of the effective aperture size and viewing angles for imaging and inversion. Here we examine the performance of the level-set-based GFWI method with a limited-aperture setup. As shown in Fig. 6, a circular void with a diameter of 1 mm (approximately $0.36\lambda_p$) and an oblique crack with a length of 1.2 mm (approximately $0.44\lambda_p$) and an orientation angle of 45°
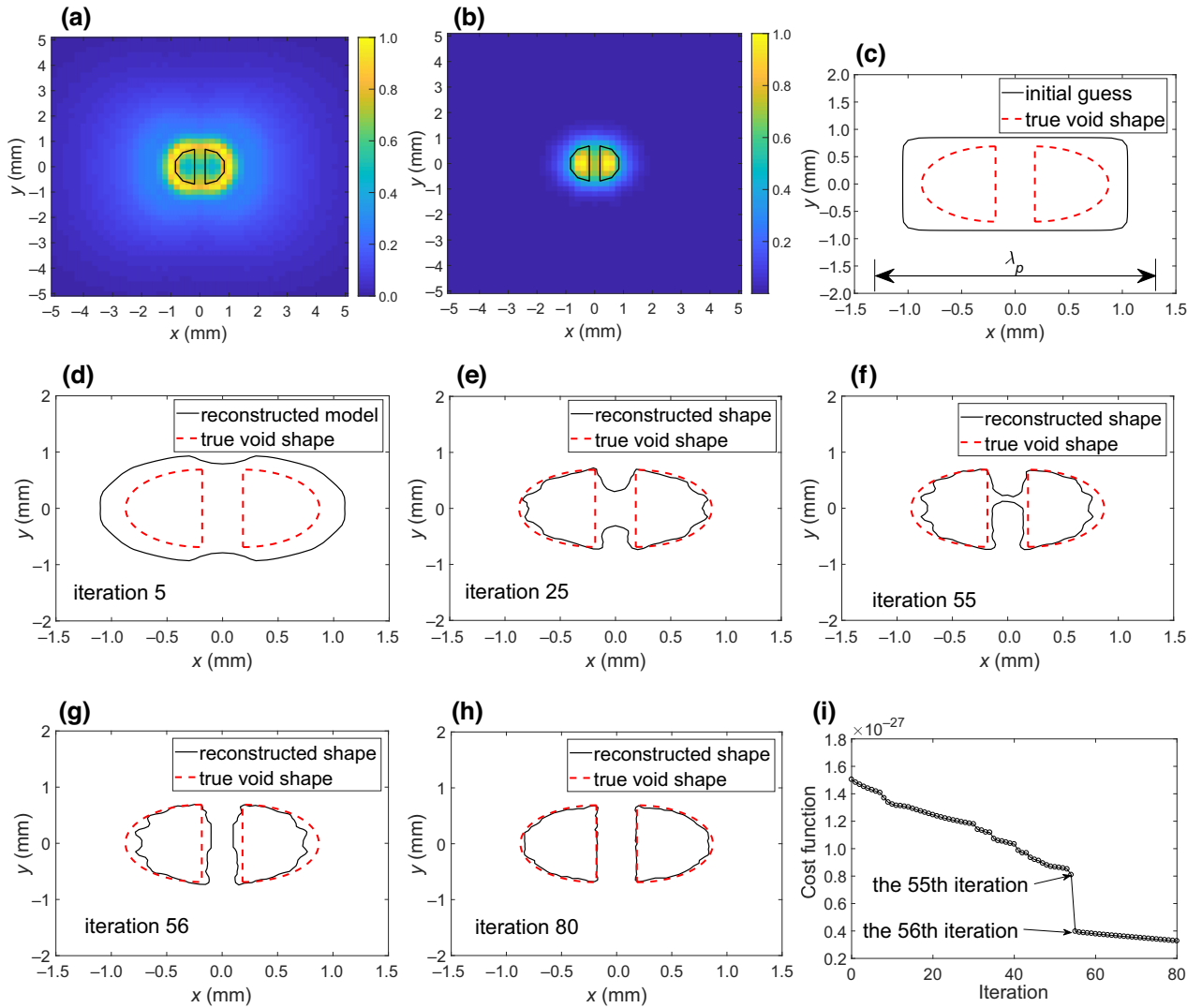
FIG. 5. Reconstruction of two subwavelength semicircular voids separated by a distance of $2\lambda_p/15$ between their inner boundaries ($\lambda_p = 2.75$ mm and $\lambda_s = 1.39$ mm). (a) The TFM image. (b) The FM image. (c) The initial model obtained from the TFM image. (d)–(h) The reconstructed shape from the 5th to the 80th iteration. (i) The cost function. The sudden drop in the cost function between the 55th and the 56th iterations corresponds to the topological change shown in (f),(g).

are placed 20 mm (approximately $7.26\lambda_p$) away from the array. The distance between the centers of the two defects is 1.2 mm (approximately $0.44\lambda_p$), and the distance between the nearest two points is only 0.28 mm (approximately $0.10\lambda_p$), far below one wavelength. We use this case to show that the method can reconstruct defects with different types and scattering features. The dimension of the FE model is 70×50 mm², and absorbing layers are placed on three sides to avoid unwanted reflection waves. A backwall is at the bottom of the FE domain, with an offset of 20 mm with respect to the defects. Reflection waves from the backwall are also used in the inversion because they provide important geometric information about the lower part of the defect not directly seen by the incident waves.

Figure 7(a) shows the TFM image of the two defects. Two objects can be vaguely identified in the image, but the types and shapes cannot be determined. After applying the -6-dB method, we can obtain an initial model containing two elliptical voids as shown in Fig. 7(b). Starting from the initial model, the shapes of the two objects are updated simultaneously as the iteration number increases. After the 20th iteration, we can see from Figs. 7(c) and 7(e) that the right-hand scatterer evolves from an elliptical void to a straight crack. The final reconstructed scatterers have almost the same shapes as the true defects as shown in Fig. 7(e). This case demonstrates the robustness of the proposed method in reconstructing defects with distinct types in a limited-aperture setup. The multiple reflections between the backwall and the scatterers are automatically
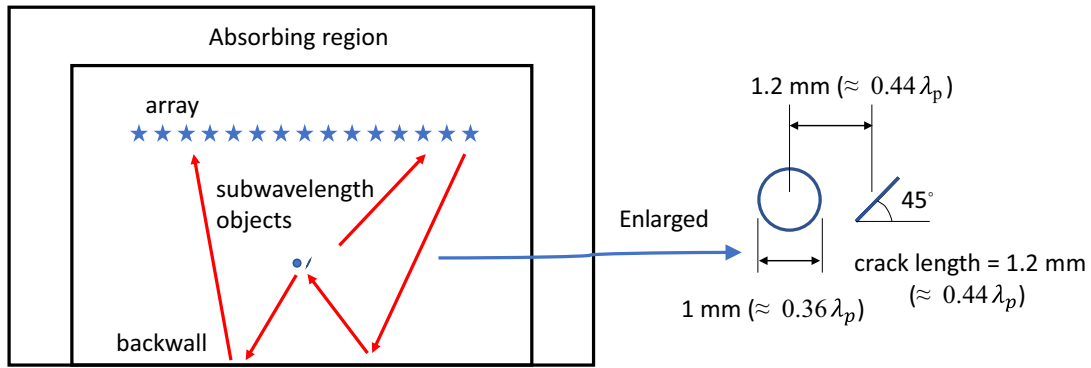
FIG. 6.   Schematic for the FE simulation of two closely spaced subwavelength defects with a backwall (limited aperture; $\lambda_p = 2.75$ mm and $\lambda_s = 1.39$ mm).

used during inversion, and hence the lower parts of the defects are accurately reconstructed.

IV. MULTIPLE VOIDS AND WAVE INTERACTION

In this section, we further explore the capability of the method in shape reconstruction of multiple closely spaced subwavelength voids. As shown in Fig. 3(d), four voids are placed in the center of the circular array with a separation distance of 0.37 mm (approximately $2/15\lambda_p$) among the inner boundaries. Each void is an isosceles right triangle with a cathetus length of 0.55 mm (approximately $1/5\lambda_p$). The geometrical features and intershape spacing

are both well below half a wavelength. The physical reason of superresolution shape reconstruction including the role of strong wave interaction and evanescent waves at the boundaries will be given using the example.

A. Reconstruction results

Figures 8(a) and 8(b) show the array images of the voids produced by TFM and FM, respectively. From both images, we can only identify one scatterer and it is almost impossible to reveal four voids especially their inner boundaries due to the resolution limit. By applying the -6-dB threshold method to Fig. 8(a), a large square void with a side length of around 2 mm is obtained as shown in Fig. 8(c), and we use it as the initial model for running
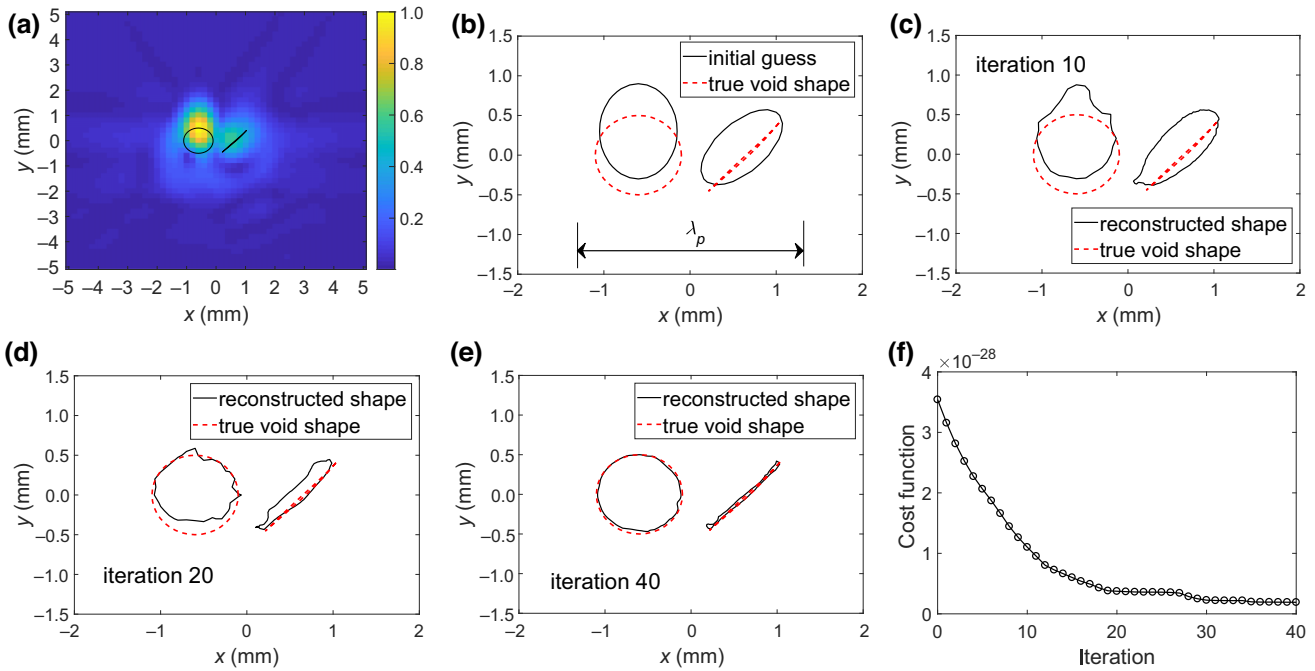

FIG. 7.   Limited-aperture reconstruction of the two subwavelength defects from Fig. 6 ($\lambda_p = 2.75$ mm and $\lambda_s = 1.39$ mm). (a) The TFM image. (b) The initial model. (c)–(e) Plots of the reconstructed shape from the 10th to the 40th iteration. (f) The cost function.

level-set-based GFWI. Note that the initial square void has a different topology and is much larger than the true voids. Even starting with a rough initial guess, the shapes of voids are correctly reconstructed as shown in Figs. 8(c)–8(j). In the first few iterations, the four sides of the initial large square contour gradually become concave, resulting in a connection area linking the four inner corners of the voids as shown in Fig. 8(e). In particular, we observe that the

connection gradually becomes a thin channel and begins to break into two parts at the 106th iteration. This indicates that the change of the topology is accurately traced during inversion, and this is also reflected as a noticeable decay in the cost function starting from the 106th iteration. At around the 118th iteration shown in Fig. 8(i), the model successfully splits into four subwavelength voids. The splitting action is consistent with a dramatic drop in the
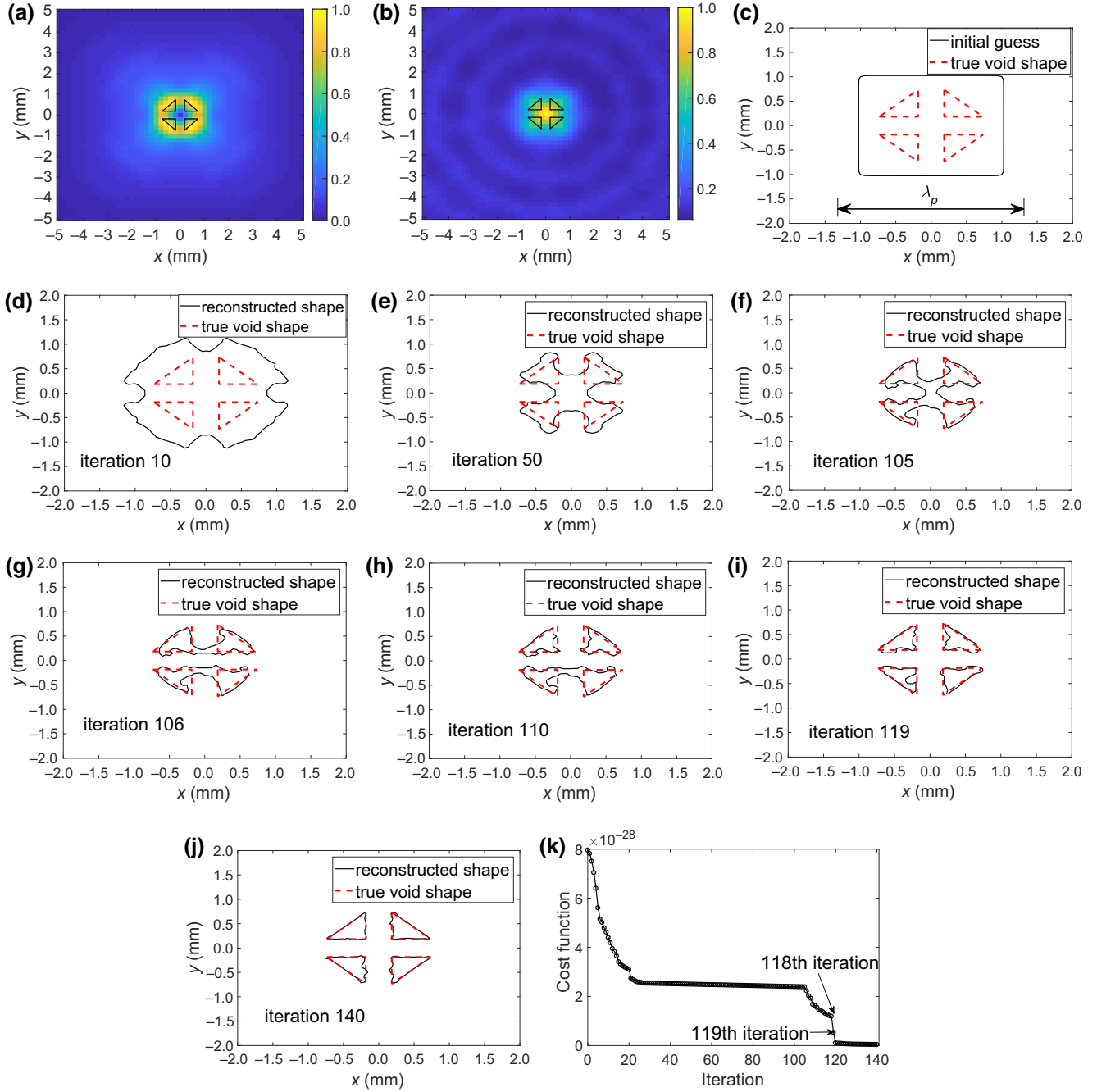

FIG. 8. Reconstruction of the four subwavelength triangular voids from Fig. 3(d) ($\lambda_p = 2.75$ mm and $\lambda_s = 1.39$ mm). (a) The TFM image. (b) The FM image. (c) The initial model. (d)–(j) Plots of the reconstructed shape from the 10th to the 140th iteration. (k) The cost function, with the drop in the cost function marked between the 118th and 119th iterations due to the topological variation.

cost function shown in Fig. 8(k). In Fig. 8(j), it can be seen that the final reconstructed shapes of the defects match very well with the true shapes, and the inner boundaries are accurately recovered.

B. Discussion

Now we discuss why the proposed method can achieve shape reconstruction of subwavelength objects separated well below half a wavelength, using the above example of four voids. The importance of taking the high-order wave interaction including evanescent waves produced within the boundary gaps into the inversion is shown.

First of all, most conventional tomography approaches seek to produce a map of material properties such as wave speed [22] or reflectivity [23], and then the shape information can be extracted based on the image contrast. To reduce the nonlinearity of the inverse problem, a linearized model (e.g., Born approximation) is often used in each iteration to invert a small update of the parameter map. This will result in the resolution being limited by half a wavelength according to small perturbation analysis
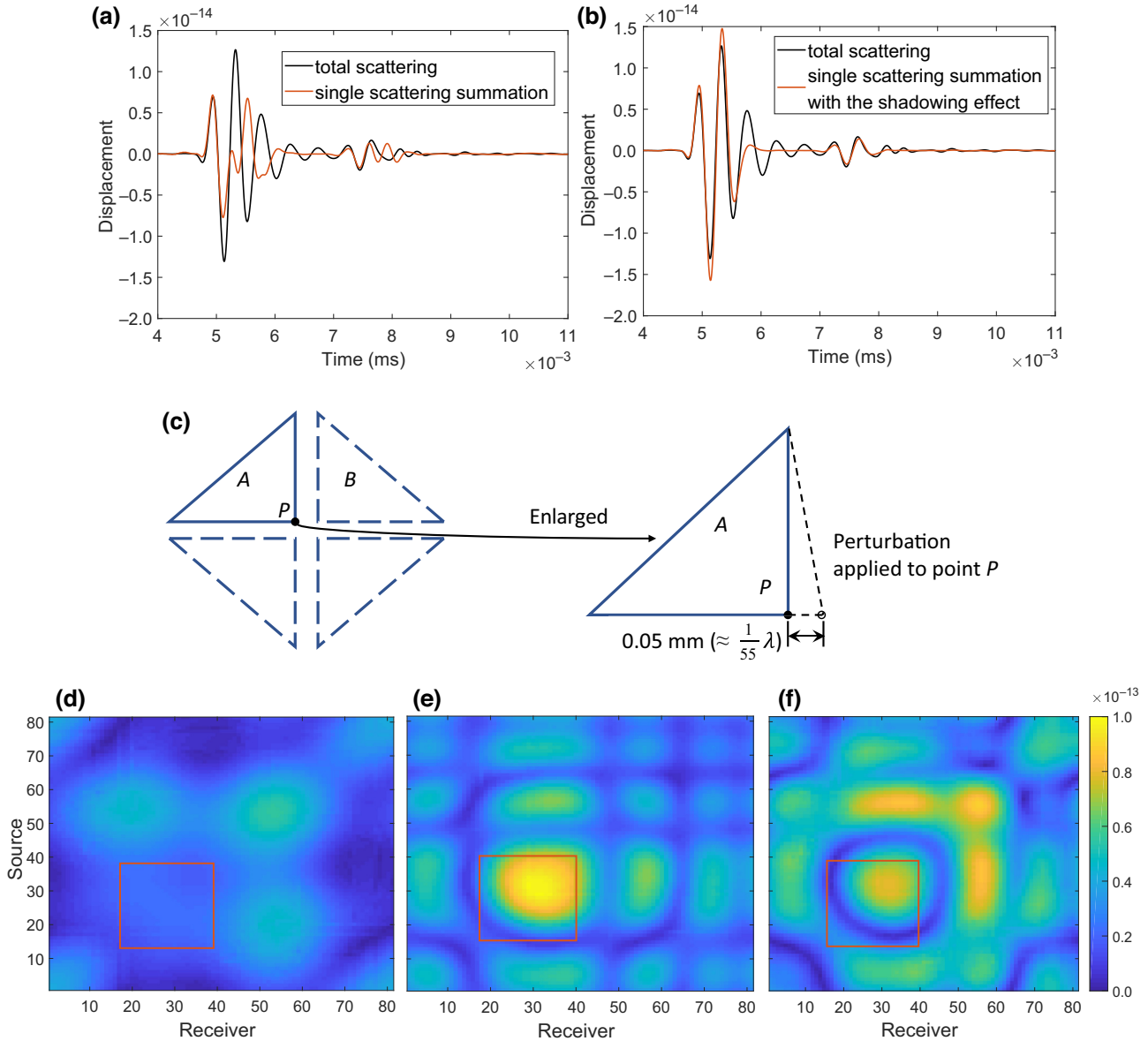

FIG. 9. Illustration of the wave interaction among the voids. (a) Comparison of the total scattering and the single scattering summation from each void for the 16th–21st source-receiver pair. (b) Comparison of the total scattering and the single scattering summation with the shadowing effects considered. (c) A small perturbation to the inner boundary of void A: the point P is moved by 0.05 mm, while the other three voids remain unchanged. (d),(e) Amplitude perturbation matrices for the single scattering and total scattering. (f) Difference between the two matrices, which represents the contribution from the wave interaction.

TABLE I.   Parameters of the ultrasonic phased array.

Number of elements per array	64	Interelement space	0.25 mm
Element width	15 mm	Center frequency	2.25 MHz
Element pitch	0.8 mm	Bandwidth (-6 dB)	1.3 MHz

[40]. Besides, most tomography methods are designed for penetrable scatterers. They have difficulties achieving convergence when the scatterers are impenetrable, because the extremely sharp material contrast creates severe local minimum problems. In contrast, level-set-based GFWI directly reconstructs the shape of the object, instead of inverting the map of material properties. It iteratively updates the boundary positions as a nonlinear shape optimization procedure, and is very suitable for impenetrable strong scatterers. The ability to reveal two very close boundaries is not restricted by the classical diffraction limit.

In addition, unlike weak penetrable scatterers, for closely spaced impenetrable scatterers the high-order wave interaction among them is non-negligible and sometimes can be as strong as the single scattering events. It is crucial to include them in the inverse model, in order to reconstruct the shapes, especially for the inner boundaries. Conventional methods based on single scattering approximations will produce incorrect images. The interior wave interaction mainly contains evanescent surface waves within the waveguide among inner boundaries. They are converted to bulk wave scattering and measured as coda waves in the far-field ultrasonic signals. These waves carry deep-subwavelength information regarding the geometrical details of the boundaries. GFWI acts as the key tool to correctly make use of these waves and hence enables superresolution shape reconstruction. To further demonstrate the important role of wave interaction, we show the simulated total scattering signal received at the 21st sensor when the 16th sensor is fired [marked as red in Fig. 3(a)]. The total signal includes both the single scattering and high-order wave interaction, and it is compared with that modeled only by the single scattering

assumptions as shown in Figs. 9(a) and 9(b). The single scattering signal in Fig. 9(a) is obtained by summing the scattered waves simulated in four individual models containing each void. It is obvious that the single scattering is very different from the total scattering signal for both the amplitude and the wave form. We also plot the single scattering signal when the geometrical shadowing effects are considered in Fig. 9(b), by only summing the scattering signals from voids A and B. The clear difference between single and total scattering indicates that the wave interaction among voids is not negligible. The level-set-based GFWI method correctly includes the high-order wave interaction in both the forward and inverse modeling, which leads to the accurate reconstruction of the inner boundaries.

We further calculate the sensitivity kernel [20,21] to examine the role of the wave interaction in shape reconstruction. The sensitivity kernel $\partial u/\partial \mathbf{m}$ quantifies the change in the received wave forms u due to a slight perturbation $\Delta \mathbf{m}$ applied to the true model [41], and it can be used to investigate the sensitivity and resolution of the imaging method. Instead of giving an explicit analytical solution, here we use the numerical method to visualize the sensitivity level of the wave interaction to the inner boundary perturbations. Specifically, the left inner boundary of void A is perturbed slightly by moving the vertex P along the x axis by 0.05 mm (approximately 0.02λ) as shown in Fig. 9(c), while the other three voids remain unchanged. The perturbation of the wave field due to the small geometrical perturbation is shown in Fig. 9(d) for single scattering and Fig. 9(e) for total scattering. We plot the matrices of perturbed scattering amplitude at the center frequency of 2.25 MHz at different transmitter-receiver pairs. As can be
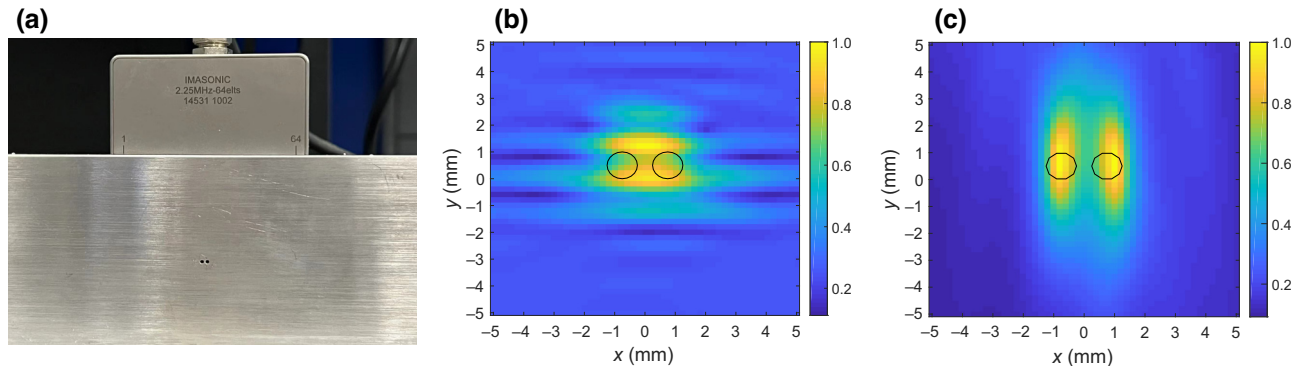

FIG. 10.   Experimental validation using an ultrasonic phased array. (a) Measurement setup with two subwavelength side-drilled holes in an aluminum block separated by 1.5 mm ($\lambda_p = 2.95$ mm). (b) The multimode TFM image. (c) The multifrequency FM image.
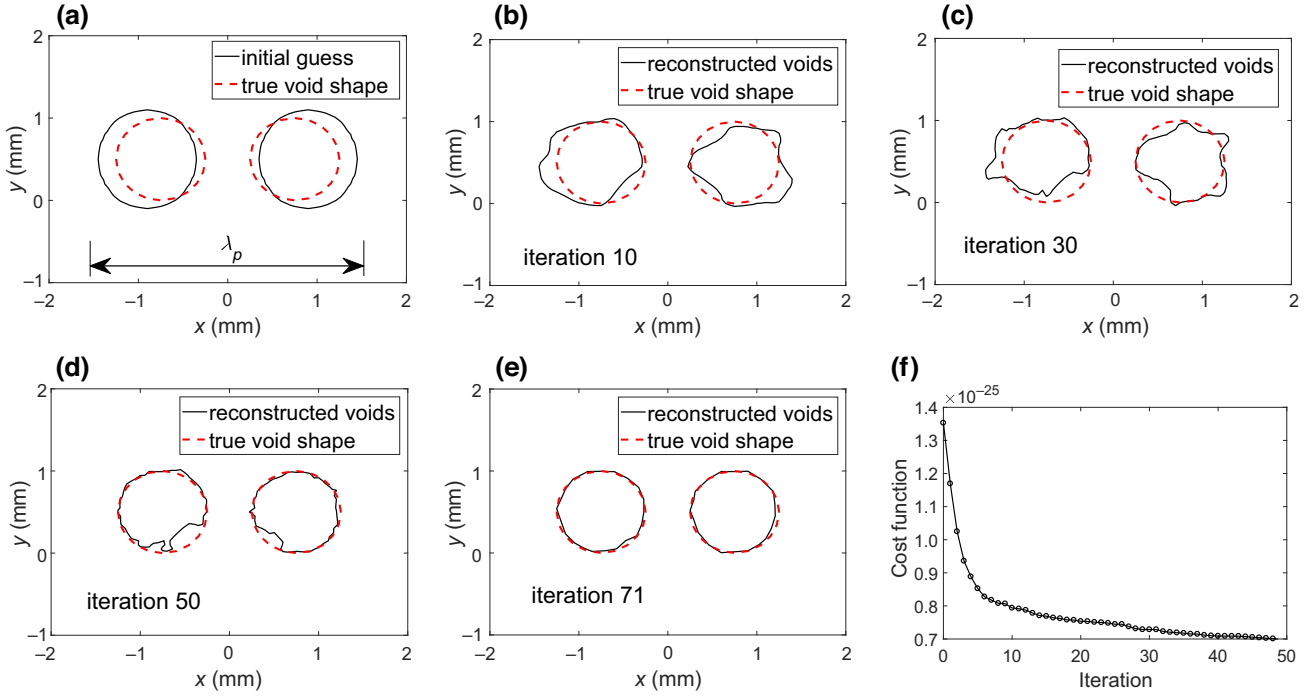
FIG. 11. Reconstruction of two subwavelength voids in the experiment ($\lambda_p = 2.95$ mm). (a) The initial model extracted from the array images in Figs. 10(c) and 10(b). (b)–(e) The reconstructed voids from the 10th to the 71st iteration. (f) The cost function.

seen, the amplitude perturbation based on the single scattering assumption is very small, which suggests that the single scattering event hardly reflects the tiny geometrical change of the inner boundaries. In contrast, the wave perturbation is much higher for the total scattering considering wave interaction among voids. In Fig. 9(e), the amplitude perturbation for transmitter-receiver pairs with element index from 15 to 40 (e.g., reflections from voids A and B) as indicated by a red square is almost four times larger than that with single scattering. The difference of the two amplitude perturbation matrices is also plotted to further show the high sensitivity of the wave interaction to the inner boundary perturbation. The comparison of the sensitivity kernels between total and single scattering implies that it is important to include the strong wave interaction in the inverse method for shape reconstruction.

V. EXPERIMENTAL VALIDATION

In addition to the above numerical simulations, we perform an experiment to further validate the capability of the proposed method in reconstructing subwavelength impenetrable objects separated within half a wavelength, when background noise is present. The experiment is conducted using a 64-element linear ultrasonic phased array (Imasonic, Besancon, France; with a Verasonics array controller system) with a center frequency of 2.25 MHz. The parameters of the array are shown in Table I. The

input signal is set to be a tone burst with a center frequency of 2.25 MHz. Each array element transmits and receives signals, and the full matrix capture of measured datasets from all transmitter-receiver pairs are recorded for postprocessing.

The array is placed tightly on the surface of an aluminum sample ($\lambda_p = 2.9$ mm), which has dimensions of $150 \times 60 \times 50$ mm^3. Two circular voids are manufactured inside the sample block via wire electrical discharging machining with a manufacturing tolerance of 0.05 mm as shown in Fig. 10(a). By using a caliper, we take several measurements of the radii and the positions of the manufactured voids to determine their true values. The two voids are located at a depth of 29.5 mm ($> 10\lambda_p$) and the radius is 0.5 mm (approximately $1/6\lambda_p$). The distance between their centers is 1.5 mm (approximately $1/2\lambda_p$). The experiment can be approximated as a 2D model, as the width of the block (50 mm) is much larger than the array width (15 mm).

We follow the same procedure as implemented in Ref. [26] to obtain the actual input signals of the phased array. A linear transfer function $H(\omega)$ is obtained by running a "twin" FE simulation with the same sample and array setups. The signals directly reflected from the backwall to the array are used to estimate the transfer function. The actual input signals can be estimated by deconvolving the measured signals with $H(\omega)$. The obtained input signals are then used in the 2D FE simulations to run the level-set-based GFWI method. The position of the
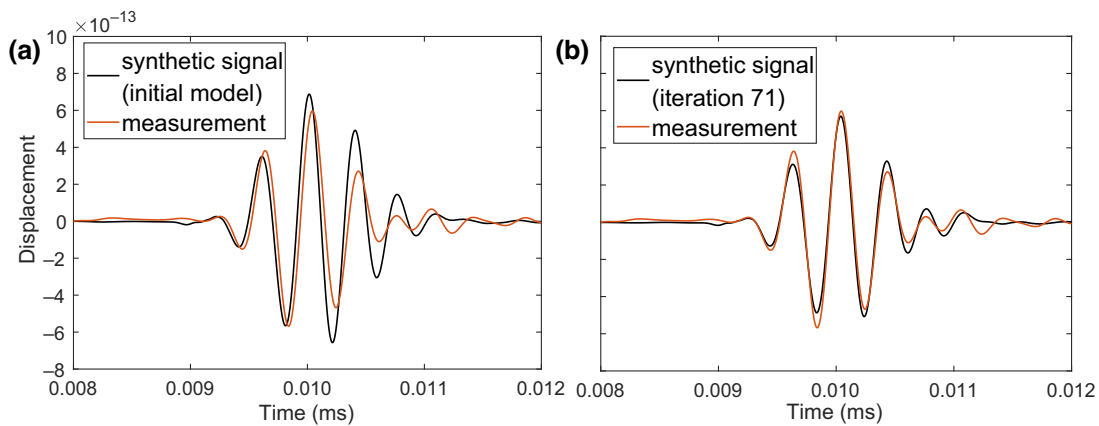
FIG. 12.   Comparison between the measurement and synthetic signals for the 32nd–33rd source-receiver pair. (a) Measurement and synthetic signals from the initial model. (b) Measurement and synthetic signals from the 71st iteration.

backwall is known beforehand. Figures 10(b) and 10(c) show the array images of the voids using the multimode TFM [42] and the multifrequency FM [15], respectively. From the TFM image, we can roughly find the upper and lower parts of the object but it is impossible to differentiate the two voids due to limited horizontal resolution. The FM image has an improved resolution and the two voids can be identified, but the actual shapes and the boundaries can be hardly revealed.

We apply the −6-dB threshold method in both images to find the approximate contours of the objects. The intersection of the two contours gives a rough estimation of the shapes, which are set as the initial geometrical model as shown in Fig. 11(a) to execute the level-set-based GFWI method. As can be observed from Figs. 11(a)–11(e), after a few iterations, the two tiny voids are accurately reconstructed and the shapes are almost the same as the ground truth. In particular, the inner boundaries of the two voids separated by $1/6\lambda$ are correctly inverted by using the proposed method. The success of the experiment demonstrates that the level-set-based GFWI method can be used for shape reconstruction of closely spaced subwavelength objects in practice.

In addition, a comparison between the measurement and the synthetic signals from the initial model and the 71st iteration is shown in Fig. 12. The signals are recorded at the 33rd sensor located at (0.4 mm, 30 mm) when the 32nd sensor at (−0.4 mm, 30 mm) is fired. A clear mismatch between the wave forms can be found in Fig. 12(a) for the initial model. After executing the shape inversion method, the simulated signal from the final iteration matches well with the experimentally measured signal as shown in Fig. 12(b).

VI. CONCLUSION AND PERSPECTIVES

In summary, we have developed a level-set-based GFWI method to achieve superresolution shape reconstruction of multiple subwavelength impenetrable objects, from far-field measurements. Most of the current far-field imaging methods obey the classic diffraction limit and cannot resolve the shapes of closely spaced objects. In particular, for impenetrable objects the high-order wave interactions can be strong. They contain important subwavelength information to reconstruct shapes (especially the inner boundaries), but these waves are often not correctly used during inversion. The method proposed in this article automatically uses all the wave physics including the interior wave interaction in calculating the correct boundary gradient. The gradient values control the evolution of boundaries for a direct reconstruction of objects with arbitrary shapes. Furthermore, by including the level-set function in shape inversion, the method can accurately capture topological changes such as splitting a single object into multiple ones and vice versa. This is a critical step to achieve superresolution capabilities. The initial image for running the shape inversion is often vague (e.g., from beamforming). With the level-set-based GFWI method, even starting from a vague contour shape, the boundaries and shapes of multiple objects can be gradually revealed by capturing the topological variation during shape optimization.

Numerical simulations with different subwavelength voids are performed and the level-set-based GFWI method successfully inverts the shapes, giving the reconstruction accuracy within a fraction of a wavelength. In particular, we show in one numerical example that the method can reconstruct the complete shapes of multiple subwavelength voids separated well below half a wavelength. The strong and complex interior wave interaction among voids is accurately captured and used in the inversion process, leading to correct inversion of the inner boundaries of voids, which are not directly probed by the incident wave. The important role of wave interaction and evanescent waves in calculating the geometrical boundary gradient is shown. In addition to the numerical simulations, an experiment is conducted using a linear ultrasonic phased

array. The shapes of closely spaced subwavelength voids are accurately inverted with the experimental data.

The proposed method enables far-field shape imaging and/or inversion of voids and defects with a deep-subwavelength resolution, which offers a powerful tool that can potentially give a step change in subsurface sensing applications such as ultrasonic nondestructive evaluation. Imaging and characterization of small defects as early as possible are crucial to mitigate the risk of component failure, and make the best use of resources during component management. Early-stage internal defects are typically much smaller than the probing wavelength and are typically of various shapes and types (e.g., straight defects, rough cracks, or voids). Geometrical information regarding size, type, and shape is challenging to determine accurately with existing approaches, which usually have a theoretical resolution limit of half a wavelength. The information provided by the level-set-based GFWI method can help significantly improve the accuracy of defect characterization, and ultimately lead to safer operation of engineering components such as those used in power plants and jet engines. For example, the method can have important applications in resolving thin microcracks with high aspect ratio, to prevent catastrophic failure of components. Lastly, the method developed here for elastic waves is versatile enough to be applied to various other applications where subsurface sensing or imaging plays a vital role. It can potentially be extended from voids and cracks to penetrable inclusions. We foresee a potential impact of this work in wave imaging such as medical ultrasound, seismology, and electromagnetic sensing.

ACKNOWLEDGMENTS

[1] L. Rayleigh, Investigations in optics, with special reference to the spectroscope, Mon. Not. R. Astron. Soc. **40,** 254 (1880).

[2] M. Slaney, A. C. Kak, and L. E. Larsen, Limitations of imaging with first-order diffraction tomography, IEEE Trans. Microw. Theory Tech. **32,** 860 (1984).

[3] A. Harootunian, E. Betzig, M. Isaacson, and A. Lewis, Super-resolution fluorescence near-field scanning optical microscopy, Appl. Phys. Lett. **49,** 674 (1986).

[4] K. P. Gaikovich, Subsurface near-field scanning tomography, Phys. Rev. Lett. **98,** 183902 (2007).

[5] C. Fan, M. Caleap, M. Pan, and B. W. Drinkwater, A comparison between ultrasonic array beamforming and super resolution imaging algorithms for non-destructive evaluation, Ultrasonics **54,** 1842 (2014).

[6] F. Shi and P. Huthwaite, Ultrasonic wave-speed diffraction tomography with undersampled data using virtual transducers, IEEE Trans. Ultrason. Ferroelectr. Freq. Control **65,** 1226 (2018).

[7] Y. Wen, H. Yu, W. Zhao, P. Li, F. Wang, Z. Ge, X. Wang, L. Liu, and W. J. Li, Scanning super-resolution imaging in enclosed environment by laser tweezer controlled superlens, Biophys. J. **119,** 2451 (2020).

[8] S. Tang, R. Wang, and J. Han, Acoustic focusing imaging characteristics based on double negative locally resonant phononic crystal, IEEE Access **7,** 112598 (2019).

[9] K. S. Rogers, K. N. Bourdakos, G. H. Yuan, S. Mahajan, and E. T. Rogers, Optimising superoscillatory spots for far-field super-resolution imaging, Opt Express **26,** 8095 (2018).

[10] T. A. Klar and S. W. Hell, Subdiffraction resolution in far-field fluorescence microscopy, Opt. Lett. **24,** 954 (1999).

[11] F. Simonetti, Localization of pointlike scatterers in solids with subwavelength resolution, Appl. Phys. Lett. **89** (2006).

[12] A. Kirsch and N. Grinberg, The factorization method for inverse problems (2007).

[13] M. Cheney, The linear sampling method and the music algorithm, Inverse Probl. **17,** 591 (2001).

[14] A. Kirsch and S. Ritter, A linear sampling method for inverse scattering from an open arc, Inverse Probl. **16,** 89 (2000).

[15] J. B. Elliott, M. J. Lowe, P. Huthwaite, R. Phillips, and D. J. Duxbury, Sizing subwavelength defects with ultrasonic imagery: An assessment of super-resolution imaging on simulated rough defects, IEEE Trans. Ultrason. Ferroelectr. Freq. Control **66,** 1634 (2019).

[16] J. Zhang, M. V. Felice, A. Velichko, and P. D. Wilcox, Angular and frequency behaviour of elastodynamic scattering from embedded scatterers, Ultrasonics **99,** 105964 (2019).

[17] E. Cardarelli, M. Cercato, A. Cerreto, and G. Di Filippo, Electrical resistivity and seismic refraction tomography to detect buried cavities, Geophys. Prospecting **58,** 685 (2010).

[18] T. Yoshihara, T. Ebihara, K. Mizutani, and Y. Sato, Underwater acoustic positioning in multipath environment using time-of-flight signal group and database matching, Jpn. J. Appl. Phys. **61,** SG1075 (2022).

[19] D. Major, D. Lenis, M. Wimmer, G. Sluiter, A. Berg, and K. Bühler, in *2020 IEEE 17th International Symposium on Biomedical Imaging (ISBI)* (IEEE, 2020), p. 1096.

[20] J. Virieux and S. Operto, An overview of full-waveform inversion in exploration geophysics, Geophysics **74,** WCC1 (2009).

[21] R. G. Pratt, C. Shin, and G. Hick, Gauss–Newton and full Newton methods in frequency–space seismic waveform inversion, Geophys. J. Int. **133,** 341 (1998).

[22] D. Borisov, F. Gao, P. Williamson, and J. Tromp, Application of 2d full-waveform inversion on exploration land data, Geophysics **85,** R75 (2020).

[23] E. Dokter, D. Köhn, D. Wilken, D. De Nil, and W. Rabbel, Full waveform inversion of sh- and love-wave data in near-surface prospecting, Geophys. Prospecting **65,** 216 (2017).

[24] V. Prieux, R. Brossier, S. Operto, and J. Virieux, Multiparameter full waveform inversion of multicomponent ocean-bottom-cable data from the valhall field. Part

1: Imaging compressional wave speed, density and attenuation, Geophys. J. Int. **194**, 1640 (2013).

[25] G. Yao, D. Wu, and S.-X. Wang, A review on reflection-waveform inversion, Pet. Sci. **17**, 334 (2020).

[26] F. Shi and P. Huthwaite, Waveform-based geometrical inversion of obstacles, Phys. Rev. Appl. **12**, 064008 (2019).

[27] P. Zuo and P. Huthwaite, Quantitative mapping of thickness variations along a ray path using geometrical full waveform inversion and guided wave mode conversion, Proc. R. Soc. A: Math., Phys. Eng. Sci. **478** (2022).

[28] X. Yin and F. Shi, Hybrid geometrical full waveform inversion for ultrasonic defect characterisation, J. Sound Vib. **535**, 117099 (2022).

[29] S. Osher and J. A. Sethian, Fronts propagating with curvature-dependent speed: Algorithms based on Hamilton-Jacobi formulations, J. Comput. Phys. **79**, 12 (1988).

[30] A. Kadu, T. van Leeuwen, and W. A. Mulder, Salt reconstruction in full-waveform inversion with a parametric level-set method, IEEE Trans. Comput. Imaging **3**, 305 (2017).

[31] W. Lewis, B. Starr, and D. Vigh, *A Level set Approach to Salt Geometry Inversion in Full-Waveform Inversion* (Society of Exploration Geophysicists, 2012), p. 1.

[32] P. Wei, Z. Li, X. Li, and M. Y. Wang, An 88-line Matlab code for the parameterized level set method based topology optimization using radial basis functions, Struct. Multidiscipl. Optim. **58**, 831 (2018).

[33] R. P. Fedkiw, T. Aslam, B. Merriman, and S. Osher, A nonoscillatory Eulerian approach to interfaces in multimaterial flows (the ghost fluid method), J. Comput. Phys. **152**, 457 (1999).

[34] E. Kansa, H. Power, G. Fasshauer, and L. Ling, A volumetric integral radial basis function method for time-dependent partial differential equations. I. Formulation, Eng. Anal. Bound. Elem. **28**, 1191 (2004).

[35] D. Adalsteinsson and J. A. Sethian, The fast construction of extension velocities in level set methods, J. Comput. Phys. **148**, 2 (1999).

[36] P. Huthwaite, Accelerated finite element elastodynamic simulations using the GPU, J. Comput. Phys. **257**, 687 (2014).

[37] R. Courant, K. Friedrichs, and H. Lewy, On the partial difference equations of mathematical physics (1986).

[38] J. R. Pettit, A. Walker, P. Cawley, and M. J. S. Lowe, A stiffness reduction method for efficient absorption of waves at boundaries for use in commercial finite element codes, Ultrasonics **54**, 1868 (2014).

[39] J. Zhang, B. W. Drinkwater, and P. D. Wilcox, The use of ultrasonic arrays to characterize crack-like defects, Journal of Nondestructive Evaluation **29**, 222 (2010).

[40] D. H. von Seggern, Spatial resolution of acoustic imaging with the Born approximation, Geophysics **56**, 1185 (1991).

[41] B. Chi, L. Dong, and Y. Liu, Correlation-based reflection full-waveform inversion, Geophysics **80**, R189 (2015).

[42] J. Zhang, B. W. Drinkwater, P. D. Wilcox, and A. J. Hunter, Defect detection using ultrasonic arrays: The multi-mode total focusing method, NDT E. Int. **43**, 123 (2010).